# Check for updates

### MECHANISTIC INTERACTIONS IN ENERGY STORAGE

# Galvanic Replacement of Magnesium Nanowire Arrays to Form Templated Antimony Frameworks

LUIS CARRILLO,  $^{1,2}$  PARKER SCHOFIELD,  $^{1,2}$  SETH ZERCHER,  $^1$  JAEHYEN JUNG,  $^1$  RACHEL DAVIDSON,  $^{1,2,3}$  and SARBAJIT BANERJEE  $^{\rm 10}$   $^{1,2,4}$ 

1.—Department of Chemistry, Texas A&M University, College Station, TX 77842-3012, USA.
2.—Department of Materials Science and Engineering, Texas A&M University, College Station, TX 77843-3003, USA. 3.—e-mail: rachelda@udel.edu.
4.—e-mail: banerjee@chem.tamu.edu

The emerging criticality of key constituents of Li-ion batteries has focused attention on more earth-abundant battery chemistries. Realizing the promise of alternative chemistries such as multivalent batteries requires the effective utilization of metal anodes. Utilization of pure magnesium as a negative electrode has been stymied by challenges such as formation of passivation layers, proclivity to form 3D deposits, and electromechanical instabilities. As such, considerable recent attention has focused on the design of composites that blend magnesium with a less electrochemically active metal. Here, we report a facile electroless galvanic replacement reaction to prepare 3D scaffolds incorporating antimony through the reaction of antimony halides with large-area electrodeposited magnesium nanowire arrays. The kinetics of the galvanic replacement reaction and the morphology of the resulting products are modulated by varying the activity coefficient and concentration of dissolved antimony-ions, which in turn is controlled through choice of the halide precursor and its solution concentration. The obtained products range from speckled antimony particles deposited across magnesium nanowires to continuous antimony scaffolds encasing electroactive magnesium cores and coreshell structures. The design of antimony-scaffolded composite architectures that nevertheless permit electrochemical accessibility of a magnesium core represents a promising scalable approach to the design of anodic frameworks.

#### INTRODUCTION

Li-ion batteries are currently the dominant rechargeable electrochemical energy storage technology owing to their superior gravimetric energy densities (in the vicinity of 300 Wh/kg for fully commercialized technologies) as well as their mature (but increasingly beleaguered) supply chains and manufacturability. L-4 Conventional Liion batteries pair transition metal oxide positive electrodes with graphite negative electrodes. Supplanting graphite with lithium metal represents a longstanding goal in anticipation of the higher accessible voltages and the order-of-magnitude

greater gravimetric and volumetric energy densities that are in principle accessible for Li metal anodes (theoretical values of 3860 Ah kg<sup>-1</sup> and 2060 Ah L<sup>-1</sup>, respectively).<sup>5,8</sup> However, despite extensive efforts, Li metal anodes have faced formidable challenges to deployment at scale because of the proclivity of the metal to deposit as dendrites as well as unresolved challenges related to large volume alterations, porosity, and pulverization, even under near-ideal plating conditions.<sup>9-11</sup> Much recent impetus in advancing Li metal anodes derives from the promise of mitigating dendrite formation by integrating solid-state electrolytes, especially in anode-free configurations, wherein Li metal is plated as needed under operational conditions.<sup>11-13</sup>

Exacerbating supply chain challenges to lithium availability as well as the emerging criticality of key elements required for conventional Li positive electrodes has focused substantial attention on alternative, more earth-abundant battery chemistries. 14,15 Many of these alternative battery chemistries continue to use graphite or alternative insertion anodes although it is clear that realizing their true promise will require effective utilization of metal anodes that afford substantially greater energy and power densities. 8,16–18 Sodium battery chemistries have advanced rapidly, even finding early market adoption, whereas challenges in materials design continue to limit the accessible energy and power densities of truly rechargeable Mg batteries.<sup>8,16–18</sup> Notably, anticipated advantages in gravimetric and volumetric densities of Mg batteries are predicated on two-electron redox in the cathode and the potential to use relatively thin film anodes while still maintaining high areal current densities.<sup>8,19</sup> Some of these benefits are negated by currently limited insertion stoichiometries, limitations in accessing broad voltage windows, and the higher mass of Mg and divalent metals compared to lithium. As such, the primary driver for divalent battery chemistries may ultimately be long-duration energy storage based primarily on considerations of cost and crustal abundance (Mg is more than 300× times as abundant as Li). Achieving uniform electroplating of Mg is further beset by numerous challenges ultimately attributable to large energy barriers to desolvation of divalent Mg-ions in liquid electrolytes, parasitic reactions resulting in the formation of passivation layers, and 3D topologies of electrodeposited products across nucleation- and diffusion-limited electrodeposition regimes.<sup>8,18,20–26</sup> These challenges, particularly the stabilization of passivating layers and sensitivity to dendrite formation, are especially acute for pure Mg metal, which otherwise has rather desirable characteristics.<sup>27</sup> For instance, Groß and co-workers noted that Mg has a lower self-diffusion barrier compared to Li including across 3D steps, which is anticipated to yield a broader operational window wherein Mg metal anodes can be uniformly plated. 10 Hagopian et al. have rationalized the observed formation of 3D morphologies of Mg through grand canonical density functional theory simulations of electro-capillary diagrams, which point to the specific roles of surface tension, potential of zero charge, and surface capacitance in governing the electrodeposited morphologies. <sup>28</sup> Consistent with previous work from our group, <sup>21</sup> thin film hexagonal platelets are predicted to be stabilized that further agglomerate to form more anisotropic 3D structures.<sup>21</sup> This view is further supported by atomistic simulations performed by Schmickler and co-workers, which consider atomicscale fluctuations that result in small excursions

from the potential of zero charge, which in turn reduces the local surface tension and drives anisotropic dendrite-like growth.<sup>29</sup>

Much current research focuses on the design of Mg electrolytes with expansive voltage windows that do not form passivating layers. 23,30-33 alternative approach has emphasized the search for alloys and composite electrodes-including architected electrodes—to sustain volume changes and pulverization accompanying metal plating and stripping. For instance, the potential of zero charge, as well as the local surface tension, is amenable to modulation through alloying<sup>29</sup> and can potentially be used in conjunction with electrolyte properties to tune electrocapillary behavior. 28 Alloying can further suppress the proclivity for surface oxidation and thereby alleviate some of the challenges arising from passivating films.<sup>27</sup> Intermetallics, alloys, and composites of Mg with several p-block elements have been examined as candidate magnesium-alloy anodes. 34-38 These materials show promising reversible Mg stripping/plating from non-aqueous electrolytes driven by stable interfaces and low-energy desolvation pathways. 39-41 The alloying element can further constitute a structural scaffold to alleviate pulverization.  $^{27,40,41}$ 

As a particularly promising alloying or compositing element, antimony shows low reversible capacity for sequestered magnesium ions (< 50 mAh g<sup>-1</sup>), which implies that a saturated, as-formed Sb-Mg alloy should remain largely inert—as needed for a deposition framework—and could thus fulfill the role of a low-volume, high-surface-area architectural template for reversible Mg plating and stripping. 41 Antimony and tin alloy anodes are indeed also at the forefront of metal anodes finding consideration in sodium batteries. 42-45 An alternative approach has focused on stabilized tailored interphases during electrochemical cycling. Recent work by Pan and co-workers demonstrates the formation of Sb/Mg interphases with precise control of thickness based on the inclusion of antimony additives in the electrolyte. 46 The presence of interphases that permit Mg-ion diffusion affords reduced overpotentials and leads to improved cyclability. Alloyed interphases are posited to suppress the formation of passivating films on the Mg anode. 47 The stabilization of Sb protective films increases lifetime, reduces proclivity for dendrite formation upon prolonged cycling, and appears to afford some degree of self-repairing ability.

Three-dimensional architected electrodes or particle geometries with morphologies that are amenable to volume changes are thought to be desirable to mitigate degradation arising from chemo-mechanical coupling, which is especially important for high-rate performance. In this work, we describe the ligand-assisted electrodeposition of Mg nanowires on metal substrates and describe a novel non-aqueous galvanic replacement route to obtain 3D Sb and Mg-Sb composite frameworks integrated

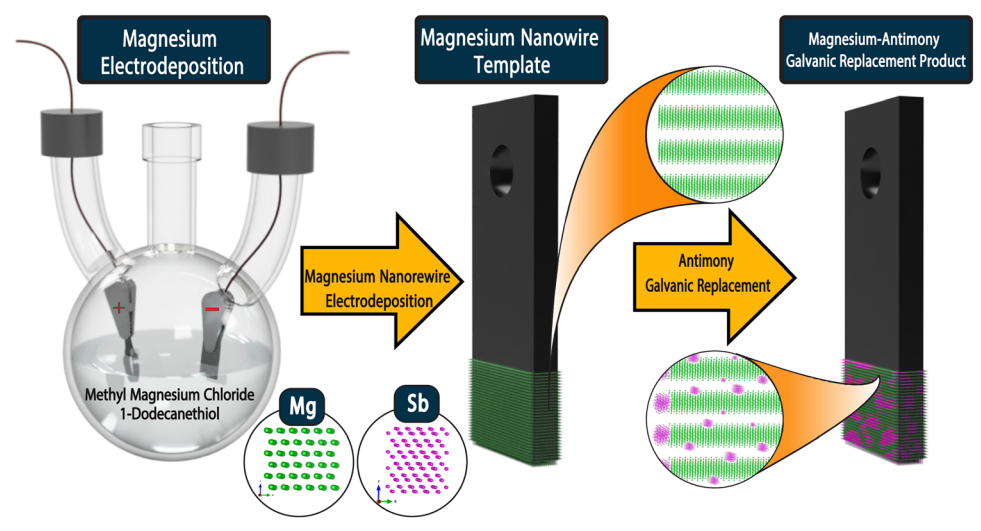


Fig. 1. General workflow of galvanic replacement. An initial ligand-assisted electrodeposition reaction is performed to electrocrystallize Mg nanowires onto a steel substrate; the nanowire array is subsequently reacted with an Sb halide precursor in a galvanic replacement reaction to form a Mg-Sb framework spanning the range from speckled coverage of Mg nanowires with Sb particles to continuous Sb shells.

onto current collectors. We present a systematic mapping of the synthetic outcomes resulting from varying the  $\mathrm{SbX}_3$  ( $X=\mathrm{Cl}$ ,  $\mathrm{Br}$ ,  $\mathrm{I}$ ) precursor, precursor concentration, and reaction time using powder X-ray diffraction and electron microscopy and demonstrate the viability of galvanic replacement as a means of constructing large-area 3D nanostructured anode arrays integrated onto current collectors. The Sb scaffold is expected to serve as a mechanically resilient framework for electrochemical cycling.

#### **EXPERIMENTAL**

## **Materials**

Synthesis of Mg Nanowire Arrays

A36 structural steel (McMaster-Carr, ASTM A36) substrates were cut into 1 cm  $\times$  2 cm coupons of 1/32" thickness. Roughly 4-mm threaded holes were bored several millimeters from the midpoint of the 1-cm edge to enable subsequent direct mounting onto magnetic substrates for imaging by scanning electron microscpy (SEM). The substrates were sanded with fine sandpaper and washed with 2-propanol and hexanes immediately prior to electrodeposition experiments.

Mg nanowires were electrodeposited onto A36 substrates following a procedure reported by Viyannalage et al.<sup>51</sup> and Davidson et al.<sup>21</sup> using a Fischer Scientific fb1000 power supply. Briefly, A36 steel substrates were placed parallel to Mg ribbons (Alfa Aesar, purity of 99.5%) in a three-neck round-bottom flask filled with 8 mL MeMgCl (Thermo Sci., 3 M in anhydrous THF) diluted with 42 mL tetrahydrofuran (THF) (DriSolv. EMD Millipore

Co., purity of  $\geq$  99.9%). The electrodes were left partially immersed in the solution, and the cell was assembled within an Ar-filled glovebox and capped with septa. Subsequently, the reaction flask was moved from the glovebox to a Schlenk line. Next, 1.5 mL 1-dodecanethiol (Thermo Sci., purity of 98%) was injected through a rubber septum. A constant current of 3 mA was applied for 4 h. After electrodeposition, the Mg nanowire arrays were gently washed with two aliquots of 15 mL THF to remove residual thiol. The samples were then dried and stored under nitrogen in a nitrogen-filled sample storage box.

# Galvanic Replacement Reactions

Magnesium nanowire arrays on A36 steel were immersed in 20 mL THF solutions containing dissolved SbCl<sub>3</sub> (Millipore Co., purity of  $\geq$  99%) at concentrations varying from 8.7 mM to 876 mM. The substrates were immersed for times ranging from 5 s to 30 s to enable galvanic replacement. Next, the supernatant was decanted and 15 mL anhydrous THF was added to quench the reaction. The supernatant was again decanted. The MgCl<sub>2</sub> product was removed by washing with deionized water ( $\rho$  = 18.2 MΩ/cm using a Barnstead International NANOpure Diamond system). The substrates were dried with nitrogen and stored under nitrogen in a nitrogen-filled sample storage box.

For reactions with SbBr<sub>3</sub> as the galvanic replacement precursor, the Mg nanowire substrates on A36 steel were immersed in 50 mL benzene (DriSolv. EMD Millipore Co., purity of  $\geq 99.8\%$ ) solutions of SbBr<sub>3</sub> (Thermo Scientific, purity of  $\geq 99.5\%$ ) with concentrations varying from 11 mM to 55 mM for 30 min to 24 h. The supernatant was decanted, and

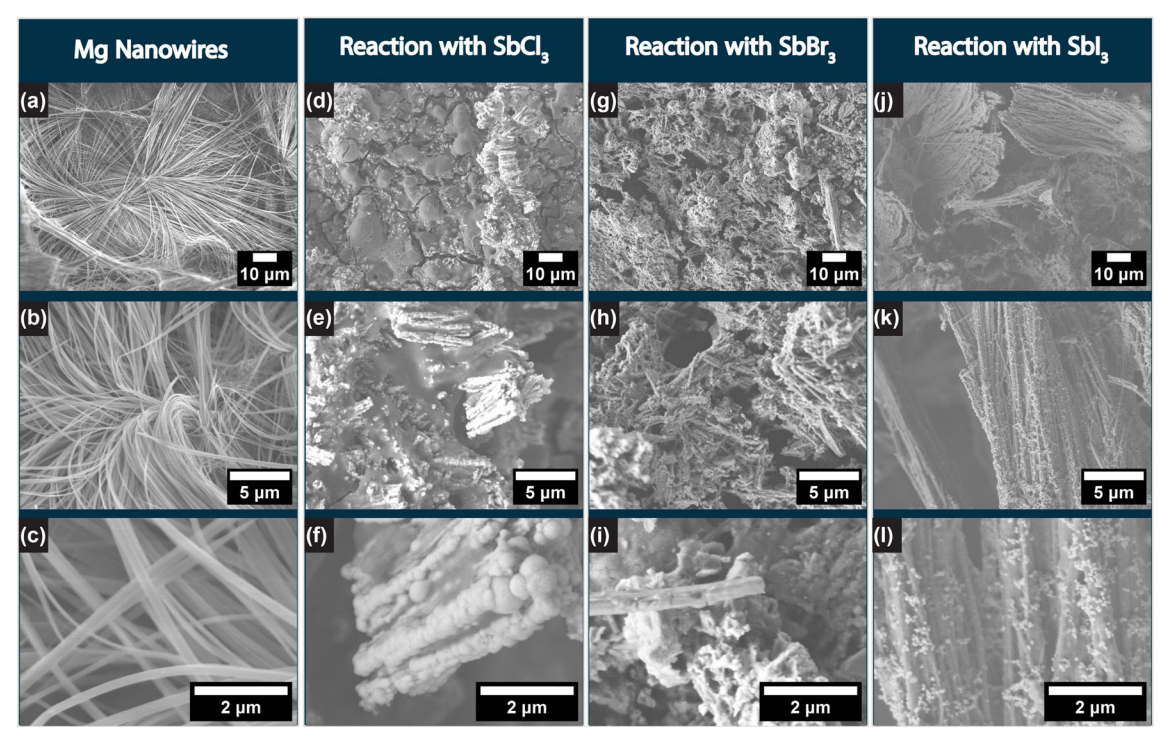


Fig. 2. SEM images comparing (a–c) array of electrodeposited Mg nanowires; (d–f) galvanic replacement products obtained after reaction with 28 mM SbCl<sub>3</sub> in THF for 30 s; (g–i) galvanic replacement products obtained after reaction with 21 mM SbBr<sub>3</sub> in benzene for 6 h; (j–l) galvanic replacement products obtained after reaction with 21 mM Sbl<sub>3</sub> in benzene for 48 h. The micrographs are acquired at increasing magnification and illustrate particles that coalesce to form agglomerated continuous shells on the surfaces of Mg nanowires.

two aliquots of 15 mL of benzene were used to remove residual surface-adsorbed SbBr $_3$ . The MgBr $_2$  product was removed by washing with 30 mL dry methanol (DriSolv EMD Millipore Co., purity of  $\geq 99.8\%$ ) for 30 min under an Ar atmosphere under Schlenk line conditions.

For reactions involving SbI<sub>3</sub>, the magnesium nanowire templates were submersed in 50 mL benzene solutions of SbI<sub>3</sub> (Millipore Co., purity of 95%) at concentrations varying from 11 mM 55 mM for 6–72 h. The solution was decanted, and two aliquots of 15 mL benzene were used to remove residual surface-adsorbed SbI<sub>3</sub>. MgI<sub>2</sub> was removed by washing with dry diethyl ether (DriSolv. EMD Millipore Co., purity of  $\geq$  99.8%) under an Ar atmosphere under Schlenk line conditions.

SEM Scanning electron Microscopy (SEM) images were acquired using a JEOL JSM-7500F instrument. Freestanding nanowires were gently spread on double-sided carbon tape attached to a commercial sample holder. A36 steel substrates were fastened to a custom-machined aluminum sample holder by one screw through the substrate bore-hole and another screw tightened over a few millimeters of the opposite substrate edge. Standard instrument conditions for imaging were 5-kV accelerating

voltage and 8-mm working distance. Energy-dispersive X-ray spectroscopy was conducted using a JEOL JSM-7500F instrument equipped with an Oxford EDX attachment. An accelerating voltage of  $10~\rm kV$  was used for the measurements.

Transmission Electron Microscopy High-resolution transmission electron microscopy (TEM) images were acquired using an FEI Titan Themis 300 S/TEM instrument. Briefly, samples were mechanically scraped from the substrate and smeared with a nitrile-gloved finger onto 400-mesh lacey-carbon films supported by copper grids (Electron Microscopy Science, Hatfield, PA). Sample-loaded grids were dried in air at room temperature. The TEM was operated at an accelerating voltage of 300 kV. STEM EDS data were acquired using a Super-X EDS detector attachment on the FEI Titan Themis 300 instrument.

Powder X-Ray Diffraction (XRD) Powder XRD data patterns were acquired using Bruker D8-Focus Bragg-Brentano X-ray powder diffractometers with Lynxeye XT or Lynxeye Detector XTE detectors. Cu K $\alpha$  radiation was used as the source in both diffractometers. Mg-Sb reaction products were scraped off the substrate in an Ar-filled glovebox

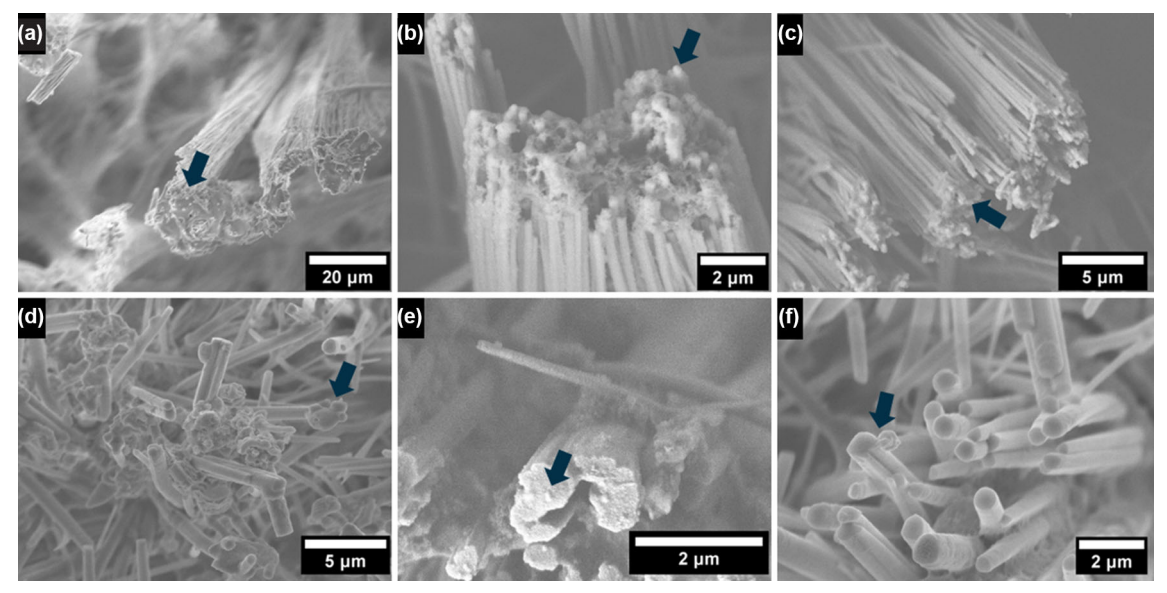


Fig. 3. SEM images of Mg nanowires reacted with (a–c) 28 mM SbBr<sub>3</sub> in benzene for 30 min and (d–f) 11 mM SbBr<sub>3</sub> in benzene for 3 h. The micrographs highlight initial Sb formation at the tips of nanowires, which are further delineated using arrows.

and placed on an air-sensitive zero background holder for analysis.

# RESULTS AND DISCUSSION

Galvanic replacement reactions involve the concurrent oxidation and dissolution of atoms from a substrate, concomitant with the reduction and deposition of atoms having a higher reduction potential. 52,53 As such, galvanic replacement reactions provide an avenue for replacement of atoms while preserving particle geometry and mesoscale electrode morphology. In this work, we demonstrate the oxidation and dissolution of metallic Mg (reduction potential for Mg $^{2+}\!/\!Mg$  is - 2.360 V versus SHE in aqueous solution at 25 °C) and the replacement of Mg atoms by solvated Sb atoms (reduction potential for  $Sb(OH)_3 + 3H^+ + 3e^- = Sb(s) + 3H_2O$  is 0.231 V versus SHE). Figure 1 illustrates the overall workflow starting with Mg nanowire arrays electrodeposited onto A36 steel. 21,55 The nanowire morphology is derived from the use of 1-dode-canethiol as a structure-directing ligand. <sup>21</sup> The nanowire array on the substrate is reacted by immersion in solutions of antimony halide salts at room temperature. The overall chemical equation can be written as:

$$\begin{aligned} &2\mathrm{Sb}X_3(\mathrm{Solv.}) + 3\mathrm{Mg}(s) \rightarrow 2\mathrm{Sb}(s) + 3\mathrm{Mg}X_2(s) \\ &X = \mathrm{Cl}, \mathrm{Br}, \ \mathrm{or} \ \mathrm{I} \end{aligned} \tag{1}$$

The aqueous equivalent  $E^0$  for this reaction is 2.591 V, which reflects a strong thermodynamic driving force for galvanic replacement. For  $M^{n+}/M$  redox couples, non-aqueous redox potentials  $E^0$ (non aq.) can be related to the aqueous reduction potential  $E^0$ (aq.) as per: $^{56,57}$ 

$$E^{0}({
m non \ aq.}) = E^{0}({
m aq.}) + {\Delta G_{t}^{0} \over nF} \eqno(2)$$

where  $\Delta G_t^0$  represents the molar Gibbs free energy of the ion being transferred from aqueous to nonaqueous solutions under standard conditions. The  $\Delta G_t^0$ value reflects the solvation energy differential.  $E^{0}$ (nonag.) will be further modified by the strength of Sb-X bands given the increasing covalency down the halide group. The overall thermodynamic driving force for galvanic replacement additionally depends on the Sb speciation in the solvent (e.g., SbX<sub>2</sub><sup>+</sup>,  $\mathrm{SbX}^{2+}$ ,  $\mathrm{Sb}^{3+}$  species), corrections to  $E^0$  (nonaq.) resulting from the chemical activity of dissolved Sb and Mg species, and complexation of dissolved Mg-ions by halide counter-ions.<sup>58</sup> As such, the antimony halide precursor and its solution concentration strongly influence the thermodynamic driving force for galvanic replacement and have been systematically varied to control the extent of Sb deposition/Mg dissolution and the morphology of the composite galvanic replacement products.

The kinetics of galvanic replacement are governed by choice of the halide precursor and reaction concentration as per:<sup>58,59</sup>

$$j_{\rm galv} = (j_{0,{
m red.}})^{eta_1} (j_{0,{
m ox.}})^{eta_2} \exp \left[ \frac{2.3(E_e^{
m red.} - E_e^{
m ox.})}{eta_{
m red.} + eta_{
m ox.}} \right] \quad (3)$$

where  $j_{\rm galv}$  is the current density arising from galvanic replacement;  $j_{0,{\rm red.}}$  and  $j_{0,{\rm ox.}}$  are the exchange current densities of the oxidation and reduction halves of Eq. 1;  $E_e^{\rm red.}$ ,  $E_e^{\rm ox.}$  are the equilibrium values of non-aqueous reduction potentials for the Sb and Mg redox couples, respectively;

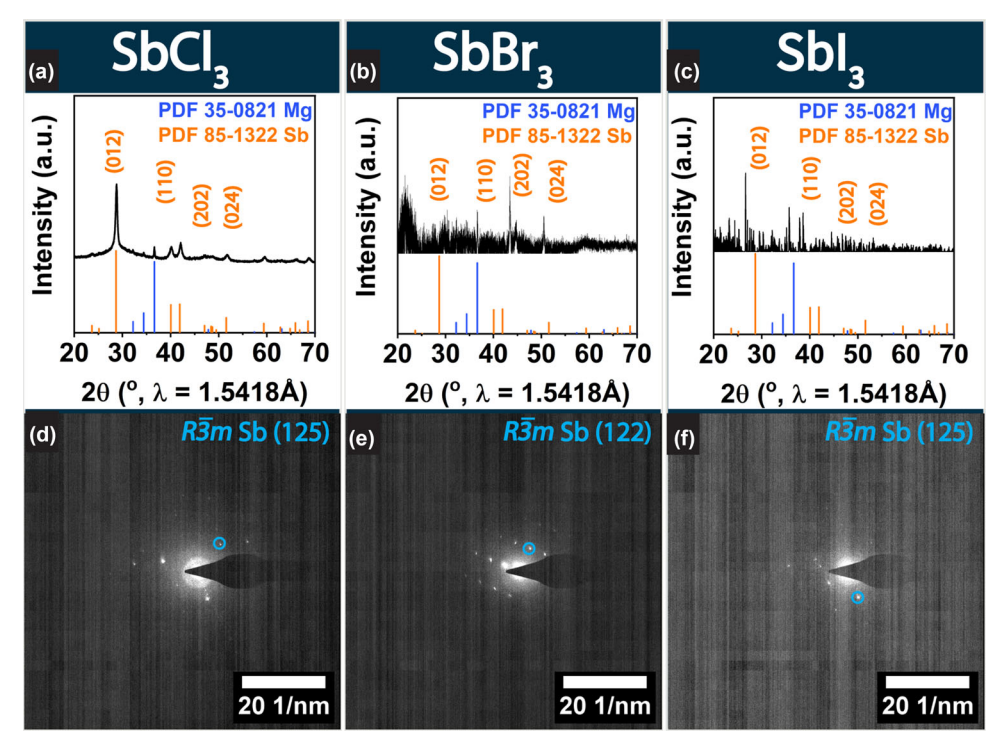


Fig. 4. Powder XRD patterns obtained after galvanic replacement reactions of Mg nanowire arrays with a (a) 28 mM solution of SbCl<sub>3</sub> in THF; (b) 55 mM solution of SbBr<sub>3</sub> in benzene; (c) 55 mM solution of Sbl<sub>3</sub> in benzene. SAED patterns acquired for galvanic replacement products obtained upon reacting Mg nanowire arrays with (d) 28 mM solution of SbCl<sub>3</sub> in THF; (e) 55 mM solution of SbBr<sub>3</sub> in benzene; (f) 55 mM solution of Sbl<sub>3</sub> in benzene.

$$\beta_1 = \frac{\beta_{\text{red.}}}{\beta_{\text{red.}} + \beta_{\text{ox.}}} \tag{4}$$

$$\beta_2 = \frac{\beta_{\text{ox.}}}{\beta_{\text{red.}} + \beta_{\text{ox.}}} \tag{5}$$

where  $\beta_{\rm red.}$ ,  $\beta_{\rm ox.}$  are Tafel slopes of the Sb<sup>3+</sup> reduction and Mg oxidation half-reactions, respectively. As such, the kinetics of deposition are further governed by the differential in non-aqueous redox potentials, which as noted above are governed by the choice of the halide precursor, precursor concentration, and dissolved anion. Ion transport of dissolved active species further plays a role in mediating the kinetics of galvanic replacement. The diffusion coefficient of antimony ions is directly proportional to the galvanic current density as well as the anionic transference number and inversely proportional to the concentration as well as the cation charge number.  $^{21,60}$ 

Electrodeposition of metallic Mg nanowires was performed as described in previous work. <sup>21</sup> Briefly, a A36 steel plate was used as the cathode and a Mg ribbon was used as the anode in a parallel plate configuration. Methyl magnesium chloride dissolved in THF is used as the electrolyte with further addition of 1-dodecanethiol as a capping ligand. The concentration and identity of the capping ligand are

integral to the formation of large-area nanowire arrays.  $^{21,61,62}$  Figure 2a, b and c shows SEM images of the Mg nanowires at different magnifications illustrating their extensive surface coverage and highly anisotropic geometry. The nanowires range from 327 nm  $\pm$  73 nm in lateral dimensions and span tens of microns in length.

As shown in Fig. 1, the Mg nanowire array is subsequently reacted in a galvanic replacement reaction by immersing the substrates in SbCl<sub>3</sub>, SbBr<sub>3</sub>, and SbI<sub>3</sub> solutions of varying concentration for different periods of time to facilitate galvanic replacement of Mg with Sb as per Eq. 1.

A first consideration in varying the antimony halide precursor used in the galvanic replacement reaction is selection of a solvent to ensure complete dissolution. THF is used as the solvent for SbCl<sub>3</sub>, whereas benzene is used to dissolve SbBr<sub>3</sub> and SbI<sub>3</sub>. Notably, the Lewis acidic nature of antimony trihalides underpins interesting reactivity with aromatic hydrocarbons (R), which are ionized as per:<sup>63</sup>

$$\begin{array}{ll} R\;(l)\;+\;2\mathrm{SbX_3(s)}\;=\;[\mathrm{RSbX_2}]^+(\mathrm{solv.})\\ &+\;\mathrm{RSbX_4^-}(\mathrm{solv.}) \end{array} \eqno(6)$$

The cationic benzene-bound Sb-species are reduced on the substrate to elemental Sb (vide infra) with concomitant oxidation of Mg. A second consideration is the removal of the  $MgX_2$  product, which precipitates from solution upon galvanic

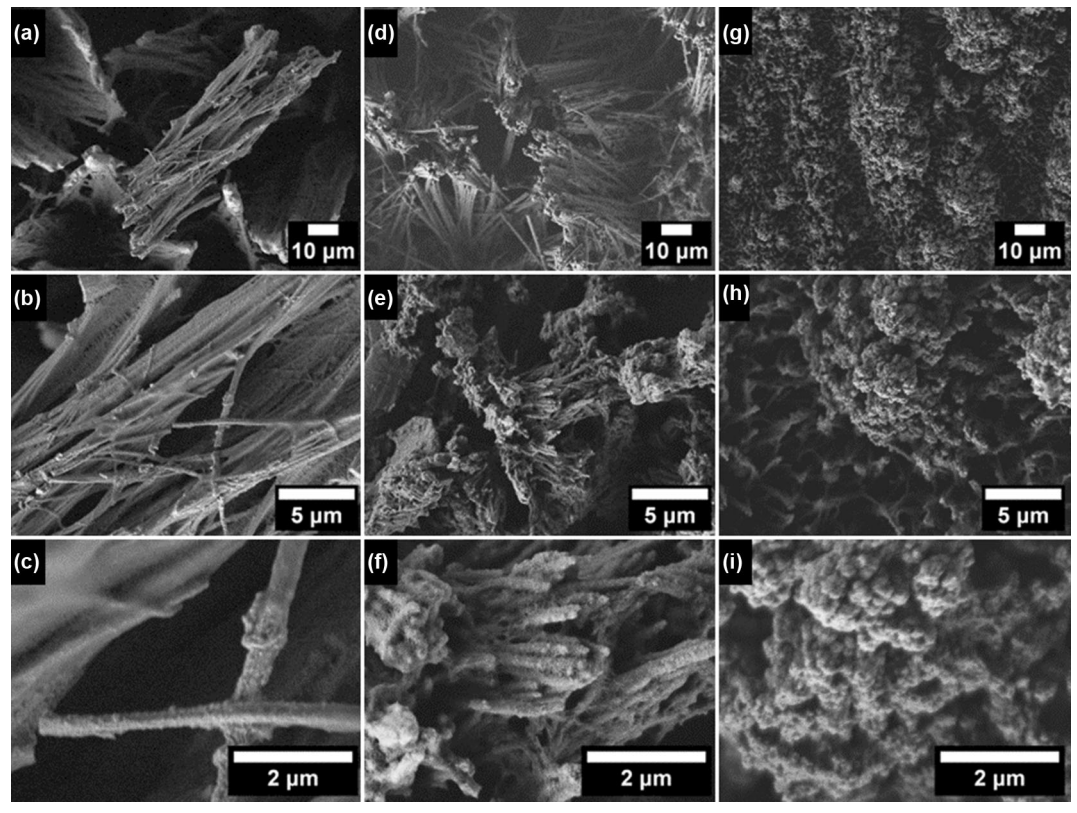


Fig. 5. SEM images of Mg nanowires at successively higher magnification after galvanic replacement reaction with SbBr<sub>3</sub> solutions in benzene at increasing concentrations from (a–c) 11 mM; (d–f) 28 mM; (g–i) 55 mM. All reactions have been performed for 6 h with subsequent washes with methanol to remove the amorphous MgBr<sub>2</sub> product.

replacement.  $MgCl_2$  is removed by washing with water, whereas  $MgBr_2$  and  $MgI_2$  are removed by washing with methanol and diethyl ether, respectively. As a third consideration, the anion transference number further affects the diffusion kinetics.

Initial galvanic replacement reactions were conducted with consistent reaction times and concentrations regarding that of SbCl3 reactions, but SbBr<sub>3</sub> and SbI<sub>3</sub> showed little to no change in Sb coverage of the Mg nanowires as a result of their much slower kinetics (Fig. S1 shows very sparse coverage at short reaction times; see online supplemental material). Thereafter, subsequent reactions were conducted with higher concentrations and more extended reaction times to obtain coverage than that obtained upon reaction with SbCl<sub>3</sub>. Figure 2 shows SEM images of galvanic replacement products obtained with the three different antimony halide precursors at comparable concentrations (2–  $3 \times 10^{-2}$  M). Almost complete coverage of Mg nanowires with Sb metal is observed within just 30 s upon reaction with SbCl<sub>3</sub>. In contrast, upon reaction with SbBr3, only partial coverage is observed after 6 h. The slowest galvanic replacement kinetics are observed with SbI3, where relatively sparse speckled coverage with Sb particles is

observed across the Mg nanowire arrays upon reaction for 48 h. Figure 2l shows high-magnification views of individual Sb particles dotting the otherwise smooth surfaces of Mg nanowires (Fig. 2c). In Fig. 2i, the product of galvanic replacement with SbBr3 shows coalescence of individual Sb particles, whereas in Fig. 2f, a continuous polycrystalline Sb shell is observed with a bamboo-like microstructure. Upon initial reaction with Sb, Mg galvanic replacement begins primarily at the faceted tips of the nanowires (Fig. 3), which are directly in contact with the antimony halide solutions. Subsequent galvanic replacement occurs throughout the stem, where individual particles coalesce upon prolonged immersion in antimony halide solutions to form a core-shell motif wherein the surface sheath comprises metallic Sb as well as adsorbed magnesium halide by-products, which are removed by solvent washing.

The observed trend in kinetics of galvanic replacement down the halide group is concordant with trends in activity coefficients measured for aqueous solutions of multivalent halides. <sup>64,65</sup> While experimental data on activity coefficients in nonaqueous media for p-block halides are exceedingly limited, the increased covalency of bonding down the halide

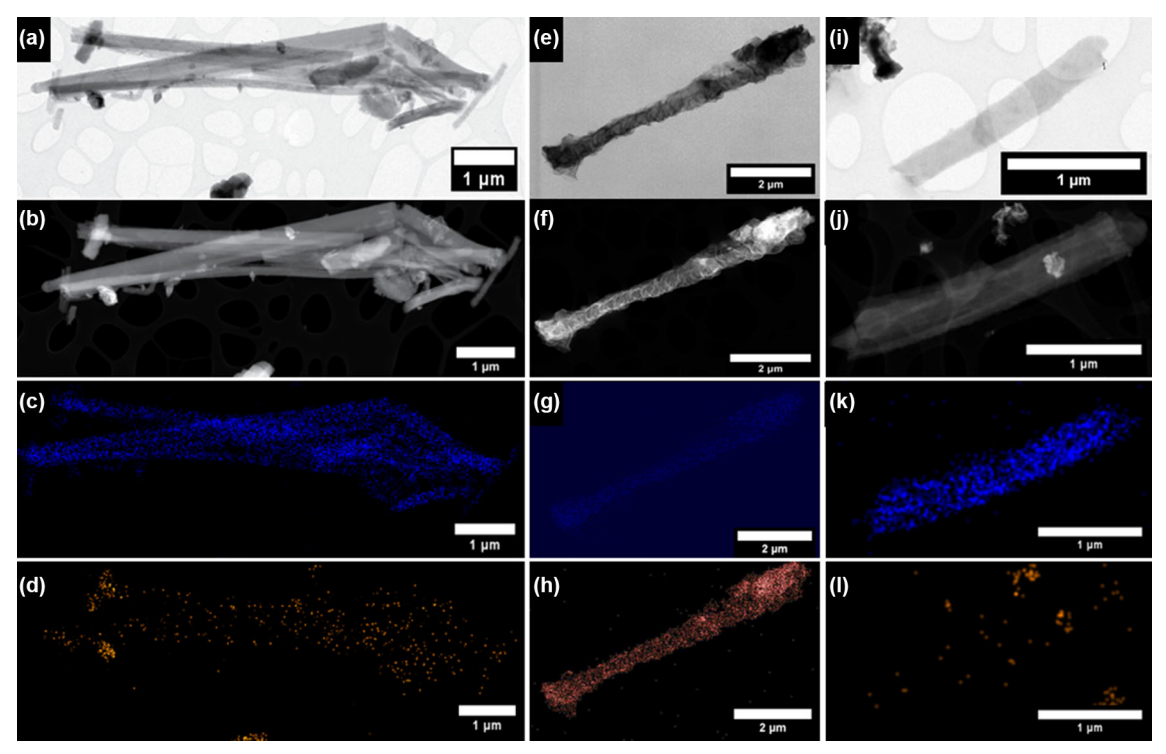


Fig. 6. Electron microscopy images and EDS maps of Mg nanowires after galvanic replacement reactions with SbBr<sub>3</sub> solutions in benzene at increasing concentrations from (a–d) 11 mM for 6 h; (e–h) 28 mM for 6 h; (i–l) 55 mM for 6 h. (a, e, i) Bright-field TEM images; (b, f, j) scanning transmission electron images; (c, g, k) Mg EDS maps; (d, h, l) Sb EDS maps showing Sb localization across Mg nanowire arrays at different concentrations.

group implies a greater proportion of undissociated ion pairs and complex ions. The higher activity coefficient of the chloride salt and the proportionately higher chemical activity thus result in a greater thermodynamic driving force for galvanic replacement based on the Nernstian correction to Eq. 2; the higher thermodynamic driving force further has the effect of directly enhancing the galvanic replacement kinetics as per Eq. 3.

Selected-area election diffraction (SAED) and powder XRD patterns have been acquired for the obtained products (Fig. 4). A powder XRD pattern acquired for the galvanic replacement product of Mg nanowires with SbCl<sub>3</sub> shown in Fig. 4A confirms the stabilization of elemental Sb crystallized in the rhombohedral phase (PDF 85-1322); reflections indexed to hexagonal Mg (PDF 35-0821) are also observed at lower intensities, which is consistent with the almost complete encasing of the Mg nanowires with an Sb shell. No other crystalline phases are observed. The powder XRD pattern for the galvanic replacement product of Mg nanowires with SbBr3 is much noisier given the sparse coverage and the relatively small volumetric fraction of surface-deposited Sb particles. Nevertheless, reflections corresponding to elemental Sb and Mg can be distinguished. The galvanic replacement product of Mg nanowires with SbI<sub>3</sub> shows reflections of elemental Sb and Mg, but reflections derived from a crystalline byproduct,  $Mg_5(IO_6)_2$  are also observed (PDF 36-0778).

Figure 5 shows SEM images of galvanic replacement products obtained by reacting Mg nanowires with 11, 28, and 55 mM solutions of SbBr<sub>3</sub> solutions in benzene. With increasing concentration, individual Sb particles nucleated onto the surfaces of Mg nanowires coalesce but do not completely replace Mg. Core-shell motifs of varying thickness are observed. Notably, at the higher concentrations examined here, the matrix increases in thickness. However, a Mg core is still retained since the surface-deposited Sb sheath acts as a barrier to further galvanic replacement. As such, the coreshell motifs provides high levels of morphological tunability. For anode applications, it is imperative to have Mg/Sb composite frameworks wherein Sb coalesces to form an electrochemically inactive structural scaffold, but all of the Mg is nevertheless electrochemically available for cycling. Galvanic replacement and Sb deposition of 28 mM SbBr3 in benzene onto Mg nanowire arrays for 6 h affords the desired morphology as illustrated in Fig. 5d, e and f.

TEM and STEM data have further been obtained for individual Mg nanowires reacted with SbBr<sub>3</sub> solutions in benzene at varying concentrations (Fig. 6). At low concentrations of SbBr<sub>3</sub> in benzene, the Mg nanowire morphology is seen to be entirely

preserved in the STEM image (Fig. 6b) and associated Mg EDS map (Fig. 6c). Sb particles are distributed across the nanowires (Fig. 6d). At high concentrations, a core-shell motif is formed wherein the Mg is fully preserved, whereas the Sb forms an encasing sheath (Fig. 6i, j, k and l). Notably, the particles and their agglomerated sheath show continuous but rounded surfaces with necking between individual Sb grains. The increased coverage of Sb and the greater extent of galvanic replacement observed with increasing SbBr3 concentration can also be traced to the Nernstian correction to Eq. 2. Increased concentration of SbBr<sub>3</sub> proportionately increases the chemical activity of dissolved Sb species, which in turn yields a higher thermodynamic driving force as per Eq. 2 as well as faster kinetics of galvanic replacement as per Eq. 3. Quantification of Sb coverage has been performed energy-dispersive X-ray spectroscopy (Table S1). Increasing concentration of the Sb precursor led to increasing Sb deposition although the matrix formation upon high Sb halide concentration led to relatively smaller changes in Sb coverage with increased Sb precursor concentration.

#### **CONCLUSION**

Unlocking the high gravimetric and volumetric energy densities of Mg metal anodes is key to realizing practical Mg battery technologies. However, despite several intrinsic advantages such as a low self-diffusion barrier, effective utilization of pure Mg metal is beset by numerous challenges including formation of passivation layers that impede Mg-ion transport, proclivity to form 3D dendritic and agglomerated platelet deposits across large operational windows, and electromechanical instabilities. Alloys, intermetallics, and composites that blend Mg with an electrochemically less active metal show promise for substantially mitigating such challenges. We demonstrate here a facile electroless galvanic replacement reaction to prepare 3D scaffolds incorporating Sb through the reaction of antimony halide salts with large-area electrodeposited Mg nanowires. The morphology of the Mg-Sb framework is substantially tunable as a function of the halide anion, precursor concentration, and reaction time. Galvanic replacement is initiated with nucleation of individual rhombohedral Sb particles onto edge facets of Mg nanowires; with subsequent galvanic replacement, Sb particles coalesce to constitute continuous shells around Mg nanowire cores. Choice of the halide anion and precursor stoichiometry provide a means of finely tuning the activity coefficient and concentration, thereby modifying the chemical activity of Sb species. The chemical activity directly impacts both the thermodynamic driving force for galvanic replacement and rate of reaction. Preservation of Mg cores and design of Sb scaffolded architectures allow for that  ${
m nevertheless}$ electrochemical

accessibility of the Mg core represent a promising scalable approach to the design of anodic frameworks. Future work will focus on pairing Sb-Mg composite anodes with liquid and solid electrolytes as well as on the use of these antimony salts in Mg electrolytes.

#### SUPPLEMENTARY INFORMATION

The online version contains supplementary material available at https://doi.org/10.1007/s11837-023-06275-7.

#### ACKNOWLEDGEMENTS

The authors gratefully acknowledge partial support from the National Science Foundation under DMR 1809866. RDD acknowledges support from the Intelligence Community Postdoctoral Research Fellowship Program administered by Oak Ridge Institute for Science and Education (ORISE) through an interagency agreement between the US Department of Energy and the Office of the Director of National Intelligence (ODNI). Use of the TAMU Materials Characterization Facility is acknowledged. The authors additionally acknowledge initial help with synthesis from Joshua Diaz.

# CONFLICT OF INTEREST

On behalf of all authors, the corresponding author states that there is no conflict of interest.

# REFERENCES

- J.U. Choi, N. Voronina, Y.K. Sun, and S.T. Myung, Adv. Energy Mater. 10, 2002027 (2020).
- N. Zhang, T. Deng, S. Zhang, C. Wang, L. Chen, C. Wang, and X. Fan, Adv. Mater. 34, 2107899 (2022).
- 3. J. Piatek, S. Afyon, T.M. Budnyak, S. Budnyk, M.H. Sipponen, and A. Slabon, *Adv. Energy Mater.* 11, 2003456 (2021).
- 4. D.A. Santos, S. Rezaei, D. Zhang, Y. Luo, B. Lin, A.R. Balakrishna, B.X. Xu, and S. Banerjee, *Chem. Sci.* 14, 458 (2022)
- Q. Zhang, W. Cai, Y.X. Yao, G.L. Zhu, C. Yan, L.L. Jiang, C. He, and J.Q. Huang, *Chem. Soc. Rev.* 49, 3806 (2020).
- L. Zhao, B. Ding, X.Y. Qin, Z. Wang, W. Lv, Y.B. He, Q.H. Yang, and F. Kang, Adv. Mater. 34, 2106704 (2022).
- H. Zhang, Y. Yang, D. Ren, L. Wang, and X. He, Energy Storage Mater 36, 147 (2021).
- Y. Liang, H. Dong, D. Aurbach, and Y. Yao, Nat. Energy 5, 646 (2020).
- Z. Huang, J. Ren, W. Zhang, M. Xie, Y. Li, D. Sun, Y. Shen, and Y. Huang, Adv. Mater. 30, 1 (2018).
- M. Jäckle, K. Helmbrecht, M. Smits, D. Stottmeister, and A. Groß, Energy Environ. Sci. 11, 3400 (2018).
- K.B. Hatzell, X.C. Chen, C.L. Cobb, N.P. Dasgupta, M.B. Dixit, L.E. Marbella, M.T. McDowell, P.P. Mukherjee, A. Verma, V. Viswanathan, A.S. Westover, and W.G. Zeier, ACS Energy Lett. 5, 922 (2020).
- L. Lin, K. Qin, Y. Sheng Hu, H. Li, X. Huang, L. Suo, and L. Chen, Adv. Mater. 34, 2110323 (2022).
- Z. Lu, Z. Yang, C. Li, K. Wang, J. Han, P. Tong, G. Li, B.S. Vishnugopi, P.P. Mukherjee, C. Yang, and W. Li, Adv. Energy Mater. 11, 2003811 (2021).

- 14. J.L. Andrews and S. Banerjee, Joule 2, 2194 (2018).
- C. Xu, Q. Dai, L. Gaines, M. Hu, A. Tukker, and B. Steubing, Commun. Mater 1, 1 (2020).
- Y. Tian, G. Zeng, A. Rutt, T. Shi, H. Kim, J. Wang, J. Koettgen, Y. Sun, B. Ouyang, T. Chen, Z. Lun, Z. Rong, K. Persson, and G. Ceder, Chem. Rev. 121, 1623 (2021).
- 17. Z. Zhao-Karger and M. Fichtner, Front. Chem. 7, 1 (2019).
- R. Mohtadi, O. Tutusaus, T.S. Arthur, Z. Zhao-Karger, and M. Fichtner, *Joule* 5, 581 (2021).
- I.D. Johnson, A.N. Mistry, L. Yin, M. Murphy, M. Wolfman, T.T. Fister, S.H. Lapidus, J. Cabana, V. Srinivasan, and B.J. Ingram, J. Am. Chem. Soc. 144, 14121 (2022).
- R. Davidson, A. Verma, D. Santos, F. Hao, C. Fincher, S. Xiang, J. Van Buskirk, K. Xie, M. Pharr, P.P. Mukherjee, and S. Banerjee, ACS Energy Lett. 4, 375 (2019).
- R. Davidson, A. Verma, D. Santos, F. Hao, C.D. Fincher, D. Zhao, V. Attari, P. Schofield, J. Van Buskirk, A. Fraticelli-Cartagena, T.E.G. Alivio, R. Arroyave, K. Xie, M. Pharr, P.P. Mukherjee, and S. Banerjee, *Mater. Horiz.* 7, 843 (2020).
- M.S. Ding, T. Diemant, R.J. Behm, S. Passerini, and G.A. Giffin, J. Electrochem. Soc. 165, A1983 (2018).
- J. Muldoon, C.B. Bucur, A.G. Oliver, T. Sugimoto, M. Matsui, H.S. Kim, G.D. Allred, J. Zajicek, and Y. Kotani, *Energy Environ. Sci.* 5, 5941 (2012).
- J.H. Kwak, Y. Jeoun, S.H. Oh, S. Yu, J.H. Lim, Y.E. Sung, S.H. Yu, and H.D. Lim, ACS Energy Lett. 7, 162 (2022).
- S.H. Yu, and H.D. Lim, ACS Energy Lett. 7, 162 (2022).
  A. Benmayza, M. Ramanathan, T.S. Arthur, M. Matsui, F. Mizuno, J. Guo, P.A. Glans, and J. Prakash, J. Phys. Chem. C 117, 26881 (2013).
- J. Eaves-Rathert, K. Moyer, M. Zohair, and C.L. Pint, *Joule* 4, 1324 (2020).
- D. Li, Y. Yuan, J. Liu, M. Fichtner, and F. Pan, J. Magnes. Alloys 8, 963 (2020).
- A. Hagopian, M.L. Doublet, and J.S. Filhol, Energy Environ. Sci. 13, 5186 (2020).
- E. Santos and W. Schmickler, Angew. Chem. Int. Ed. 60, 5876 (2021).
- H.D. Yoo, I. Shterenberg, Y. Gofer, G. Gershinsky, N. Pour, and D. Aurbach, Energy Environ. Sci. 6, 2265 (2013).
- O. Tutusaus, R. Mohtadi, T.S. Arthur, F. Mizuno, E.G. Nelson, and Y.V. Sevryugina, Angew. Chem. 127, 8011 (2015).
- W. Sun, L. Chen, J. Wang, H. Zhang, Z. Quan, F. Fu, H. Kong, S. Wang, and H. Chen, J. Mater. Chem. A. Mater. 11, 15724 (2023).
- 33. K.L. Ng, K. Shu, and G. Azimi, *IScience* 25, 104711 (2022).
- Y.H. Tan, W.T. Yao, T. Zhang, T. Ma, L.L. Lu, F. Zhou, H. Bin Yao, and S.H. Yu, ACS Nano 12, 5856 (2018).
- F. Murgia, P-Block Elements as Negative Electrode Materials for Magnesium-Ion Batteries: Electrochemical Mechanism and Performance (2016).
- L. Blondeau, E. Foy, H. Khodja, and M. Gauthier, J. Phys. Chem. C 123, 1120 (2019).
- B. Huang, Z. Pan, X. Su, and L. An, J. Power. Sources 395, 41 (2018).
- F. Murgia, L. Stievano, L. Monconduit, and R. Berthelot, J. Mater. Chem. A. Mater. 3, 16478 (2015).
- N. Wu, Y.C. Lyu, R.J. Xiao, X. Yu, Y.X. Yin, X.Q. Yang, H. Li, L. Gu, and Y.G. Guo, NPG Asia Mater. 6, 1 (2014).
- Y. Shao, M. Gu, X. Li, Z. Nie, P. Zuo, G. Li, T. Liu, J. Xiao, Y. Cheng, C. Wang, J.G. Zhang, and J. Liu, *Nano Lett.* 14, 255 (2014).
- Y. Cheng, Y. Shao, L.R. Parent, M.L. Sushko, G. Li, P.V. Sushko, N.D. Browning, C. Wang, and J. Liu, Adv. Mater. 27, 6598 (2015).

- K. Nieto, D.S. Windsor, A.R. Kale, J.R. Gallawa, D.A. Medina, and A.L. Prieto, *J. Phys. Chem. C* 127, 12415 (2023)
- S. Sarkar, H.J. Gonzalez-Malabet, M. Flannagin, A. L'Antigua, P.D. Shevchenko, G.J. Nelson, P.P. Mukherjee, and A.C.S. Appl, *Mater. Interfaces* 14, 29711 (2022).
- 44. K. Nieto, N.J. Gimble, L.J. Rudolph, A.R. Kale, and A.L. Prieto, J. Electrochem. Soc. 169, 050537 (2022).
- S. Sarkar, A. Verma, and P.P. Mukherjee, J. Electrochem. Soc. 168, 090550 (2021).
- B. Yang, L. Xia, R. Li, G. Huang, S. Tan, Z. Wang, B. Qu, J. Wang, and F. Pan, J. Mater. Sci. Technol. 157, 154 (2023).
- J. Zhang, X. Guan, R. Lv, D. Wang, P. Liu, and J. Luo, Energy Stor. Mater. 26, 408 (2020).
- Y. Zhao, P. Stein, Y. Bai, M. Al-Siraj, Y. Yang, and B.X. Xu, J. Power. Sources 413, 259 (2019).
- L.S. De Vasconcelos, R. Xu, Z. Xu, J. Zhang, N. Sharma, S.R. Shah, J. Han, X. He, X. Wu, H. Sun, S. Hu, M. Perrin, X. Wang, Y. Liu, F. Lin, Y. Cui, and K. Zhao, Chem. Rev. 122, 13043 (2022).
- J.L. Andrews, P. Stein, D.A. Santos, C.J. Chalker, L.R. De Jesus, R.D. Davidson, M.A. Gross, M. Pharr, J.D. Batteas, B.-X. Xu, and S. Banerjee, *Matter* 3, 1754 (2020).
- L. Viyannalage, V. Lee, R.V. Dennis, D. Kapoor, C.D. Haines, and S. Banerjee, Chem. Comm. 48, 5169 (2012).
- M.H. Oh, T. Yu, S.-H. Yu, B. Lim, K.-T. Ko, M.-G. Willinger, D.-H. Seo, B.H. Kim, M.G. Cho, J.-H. Park, K. Kang, Y.-E. Sung, N. Pinna, and T. Hyeon, *Science* (1979) 340, 964 (2013).
- H. Cheng, C. Wang, D. Qin, and Y. Xia, Acc. Chem. Res. 56, 900 (2023).
- 54. S.G. Bratsch, J. Phys. Chem. Ref. Data 18, 1 (1989).
- L. Viyannalage, V. Lee, R.V. Dennis, D. Kapoor, C.D. Haines, and S. Banerjee, Chem. Commun. 48, 5169 (2012).
- J. Hwang, T. Yamamoto, A. Sakuda, K. Matsumoto, and K. Miyazaki, *Electrochemistry* 90, 102002 (2022).
- 57. Y. Marcus, Pure Appl. Chem. 57, 1129 (1985).
- A. Papaderakis, I. Mintsouli, J. Georgieva, and S. Sotiropoulos, Catalysts 7, 80 (2017).
- W.F.C. Pletcher, *Industrial Electrochemistry II* (Chapman & Hall, London, 1990).
- F. Hao, A. Verma, and P.P. Mukherjee, *Energy Stor. Mater.* 20, 1 (2019).
- 61. X. Liu, M. Atwater, J. Wang, and Q. Huo, Colloids Surf. B Biointerfaces 58, 3 (2007).
- L.M. Rossi, J.L. Fiorio, M.A.S. Garcia, and C.P. Ferraz, *Dalton Trans.* 47, 5889 (2018).
- P.V. Johnson and E.C. Baughan, J. Chem. Soc. A: Inorgan. Phys. Theor. https://doi.org/10.1039/J19690002686 (1969).
- 64. W.W. Lucasse, J. Am. Chem. Soc. 51, 2597 (1929).
- 65. F.H. Getman, J. Phys. Chem. 32, 940 (1928).

**Publisher's Note** Springer Nature remains neutral with regard to jurisdictional claims in published maps and institutional affiliations.

Springer Nature or its licensor (e.g. a society or other partner) holds exclusive rights to this article under a publishing agreement with the author(s) or other rightsholder(s); author self-archiving of the accepted manuscript version of this article is solely governed by the terms of such publishing agreement and applicable law.